A coherent spin–photon interface in silicon

X. Mi[1], M. Benito[2], S. Putz[1], D. M. Zajac[1], J. M. Taylor[3], Guido Burkard[2] & J. R. Petta[1]

Electron spins in silicon quantum dots are attractive systems for quantum computing owing to their long coherence times and the promise of rapid scaling of the number of dots in a system using semiconductor fabrication techniques. Although nearest-neighbour exchange coupling of two spins has been demonstrated, the interaction of spins via microwave-frequency photons could enable long-distance spin–spin coupling and connections between arbitrary pairs of qubits ('all-to-all' connectivity) in a spin-based quantum processor. Realizing coherent spin–photon coupling is challenging because of the small magnetic-dipole moment of a single spin, which limits magnetic-dipole coupling rates to less than 1 kilohertz. Here we demonstrate strong coupling between a single spin in silicon and a single microwave-frequency photon, with spin–photon coupling rates of more than 10 megahertz. The mechanism that enables the coherent spin–photon interactions is based on spin–charge hybridization in the presence of a magnetic-field gradient. In addition to spin–photon coupling, we demonstrate coherent control and dispersive readout of a single spin. These results open up a direct path to entangling single spins using microwave-frequency photons.

Solid-state electron spins and nuclear spins are quantum mechanical systems that can be almost completely isolated from environmental noise. As a result, they have coherence times as long as hours and so are one of the most promising types of quantum bit (qubit) for constructing a quantum processor[1–3]. On the other hand, this degree of isolation poses difficulties for the spin–spin interactions that are needed to implement two-qubit gates. So far, most approaches have focused on achieving spin–spin coupling through the exchange interaction or the much weaker dipole–dipole interaction[4–6]. Among existing classes of spin qubits, electron spins in gate-defined silicon quantum dots have the advantages of scalability due to mature fabrication technologies and low dephasing rates due to isotopic purification[7]. Currently, silicon quantum dots are capable of supporting fault-tolerant control fidelities for single-qubit gates and high-fidelity two-qubit gates based on exchange[8–12]. Coupling of spins over long distances has been pursued through the physical displacement of electrons[13–16] and through 'super-exchange' via an intermediate quantum dot[17]. The recent demonstration of strong coupling between the charge state of a quantum-dot electron and a single photon has raised the prospect of strong spin–photon coupling, which could enable photon-mediated long-distance spin entanglement[18–20]. Spin–photon coupling may be achieved by coherently hybridizing spin qubits with photons trapped inside microwave cavities, in a manner similar to cavity quantum electrodynamics with atomic systems and circuit quantum electrodynamics with solid-state qubits[19–25]. Such an approach, however, is extremely challenging: the small magnetic moment of a single spin leads to magnetic-dipole coupling rates of 10–150 Hz, which are far too slow compared with electron-spin dephasing rates to enable a coherent spin–photon interface[25–30].

Here, we resolve this outstanding challenge by using spin–charge hybridization to couple the electric field of a single photon to a single spin in silicon[25,31–34]. We measure spin–photon coupling rates $g_s/(2\pi)$ of up to 11 MHz, nearly five orders of magnitude higher than typical magnetic-dipole coupling rates. These values of $g_s/(2\pi)$ exceed both the photon decay rate $\kappa/(2\pi)$ and the spin decoherence rate $\gamma_s/(2\pi)$, firmly anchoring our spin–photon system in the strong-coupling regime[26,29,30].

Our coupling scheme consists of two stages of quantum-state hybridization. First, a single electron is trapped within a gate-defined silicon double quantum dot (DQD) that has a large electric-dipole moment. A single photon confined within a microwave cavity hybridizes with the electron charge state through the electric-dipole interaction[35,36]. Second, a micrometre-scale magnet (micromagnet) placed over the DQD hybridizes electron charge and spin by producing an inhomogeneous magnetic field[31–34]. The combination of the electric-dipole interaction and spin–charge hybridization gives rise to a large effective spin–photon coupling rate. At the same time, the relatively low level of charge noise in the device ensures that the effective spin decoherence rate γ_s remains below the coherent coupling rate g_s—a criterion that has hampered previous efforts to achieve strong spin–photon coupling[37].

As well as demonstrating a coherent spin–photon interface, we also show that our device architecture is capable of single-spin control and readout. Single-spin rotations are electrically driven[9,38] and the resulting spin state is detected through a dispersive phase shift in the cavity transmission, which reveals Rabi oscillations[36].

Spin–photon interface

The device that enables strong spin–photon coupling is shown in Fig. 1a and contains two gate-defined DQDs fabricated using an overlapping aluminium gate stack (Fig. 1b). The gates are electrically biased to create a double-well potential that confines a single electron in the underlying natural-silicon quantum well (Fig. 1c). A plunger gate (P2) on each DQD is connected to the centre pin of a half-wavelength niobium superconducting cavity with a centre frequency of $f_c = 5.846$ GHz and quality factor of $Q_c = 4{,}700$ ($\kappa/(2\pi) = f_c/Q_c = 1.3$ MHz), which hybridizes the electron charge state with a single cavity photon through the electric-dipole interaction[18–20,35,36]. Because the spin–photon coupling rate g_s is directly proportional to the charge–photon coupling rate g_c (refs 25, 31–34, 39–41), we have modified the cavity dimensions

[1]Department of Physics, Princeton University, Princeton, New Jersey 08544, USA. [2]Department of Physics, University of Konstanz, D-78464 Konstanz, Germany. [3]Joint Quantum Institute/NIST, College Park, Maryland 20742, USA.

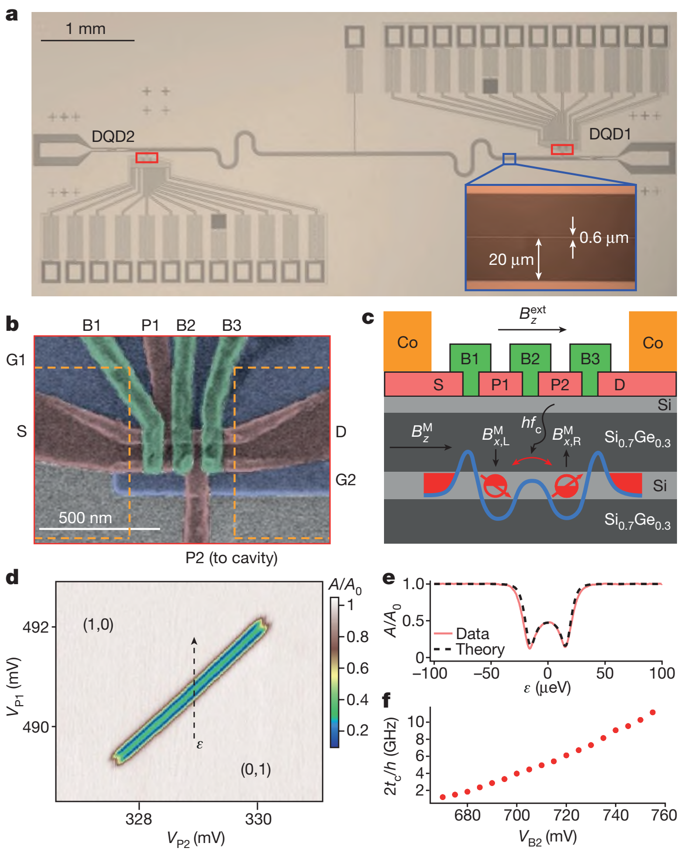

Figure 1 | Spin–photon interface. a, Optical image of the superconducting microwave cavity. The inset shows an optical image of the centre pin (0.6 μm) and vacuum gap (20 μm) of the cavity. **b**, False-colour scanning electron micrograph (SEM) of a DQD. Gate electrodes are labelled as G1, G2, S, D, B1, P1, B2, P2 and B3, where G1 and G2 are screening gates, S and D are used for accumulating electrons in the source and drain reservoirs, and B1 and B3 control the tunnel barrier of each dot to its adjacent reservoir. The locations of the cobalt micromagnets are indicated by the orange dashed lines. **c**, Schematic cross-sectional view of the DQD device. The blue line indicates the electrostatic confinement potential which delocalizes a single electron between the two dots (indicated as half-filled circles). The quantization axis of the electron spin (red arrow) changes between the dots. **d**, Cavity transmission amplitude A/A_0 at $f = f_c$, where f_c is the centre frequency of the cavity, near the (1, 0) ↔ (0, 1) inter-dot transition for DQD1, plotted as a function of the voltages on gates P1 and P2, V_{P1} and V_{P2}, with $B_z^{ext} = 0$ and $V_{B2} = 710$ mV. The dashed arrow denotes the DQD detuning parameter ε, which is equal to the difference in the chemical potentials of the two dots and points along the vertical direction because in this work V_{P1} is changed to vary ε. V_{B2} denotes the voltage on gate B2, which controls the inter-dot tunnel coupling t_c. **e**, A/A_0 as a function of ε with $V_{B2} = 710$ mV (red line) and a fit to cavity input–output theory (black dashed line), with $g_c/(2\pi) = 40$ MHz. **f**, $2t_c/h$ as a function of V_{B2} for DQD1, obtained by measuring $A(\varepsilon)/A_0$ at different values of V_{B2}.

(Fig. 1a, inset) to achieve a high characteristic impedance Z_r and therefore a high g_c ($g_c \propto \sqrt{Z_r}$; ref. 20). To hybridize the charge state of the trapped electron with its spin state, a cobalt micromagnet is fabricated near the DQD, which generates an inhomogeneous magnetic field. For our device geometry, the magnetic field due to the cobalt micromagnet has a component along the z axis B_z^M that is approximately constant for the DQD and a component along the x axis that takes on an average value of $B_{x,L}^M$ ($B_{x,R}^M$) for the left (right) dot (Fig. 1c, Extended Data Fig. 1). The relatively large field difference $B_{x,R}^M - B_{x,L}^M = 2B_x^M$ leads to spin–charge hybridization, which, when combined with charge–photon coupling, gives rise to spin–photon coupling[33,34].

We first characterize the strength of the charge–photon interaction, because this sets the scale of the spin–photon interaction rate. For simplicity, only one DQD is active at a time for all of the measurements presented here. The cavity is driven by a coherent microwave tone at frequency $f = f_c$ and power $P \approx -133$ dBm (corresponding to approximately 0.6 photons in the cavity, determined on the basis of AC Stark shift measurements of the spin-qubit frequency in the dispersive regime; see Extended Data Fig. 2)[42]. The normalized cavity transmission amplitude A/A_0 is displayed in Fig. 1d as a function of the voltages V_{P1} and V_{P2} on gates P1 and P2 of the first DQD (DQD1), which reveals the location of the (1, 0) ↔ (0, 1) inter-dotcharge transition (see Extended Data Fig. 3 for overall stability diagrams)[18–20,35,36]. Here (n, m) denotes a charge state, with the number of electrons in the left (P1) and right (P2) dot being n and m, respectively. The charge–photon coupling rate is estimated quantitatively by measuring A/A_0 as a function of the DQD level detuning ε (Fig. 1e). By fitting the data with the cavity input–output theory model using $\kappa/(2\pi) = 1.3$ MHz, we find $g_c/(2\pi) = 40$ MHz and $2t_c/h = 4.9$ GHz, where t_c is the inter-dot tunnel coupling and h is the Planck constant[19,36,37]. A charge decoherence rate of $\gamma_c/(2\pi) = 35$ MHz is also estimated from the fit and confirmed independently using microwave spectroscopy with $2t_c/h = 5.4$ GHz (refs 19, 20, 42). Fine control of the DQD tunnel coupling, which is critical for achieving spin–charge hybridization[33], is shown in Fig. 1f, in which $2t_c/h$ is plotted as a function of the voltage V_{B2} on the inter-dot barrier gate B2. A similar characterization of the second DQD (DQD2) yields $g_c/(2\pi) = 37$ MHz and $\gamma_c/(2\pi) = 45$ MHz at the (1, 0) ↔ (0, 1) inter-dot charge transition. Owing to the higher impedance of the resonator, the values of g_c measured here are much larger than in previous silicon DQD devices[19,43], which is helpful for achieving strong spin–photon coupling. In general, there are device-to-device variations in γ_c (refs 19, 43). It is unlikely the slightly higher charge decoherence rate is a result of our cavity design, because the Purcell decay rate[29] is estimated to be $\Gamma_c/(2\pi) \approx 0.02$ MHz $\ll \gamma_c/(2\pi)$. Excited valley states are not visible in the cavity response of either DQD, suggesting that they have negligible population[44]. We therefore exclude valleys from the analysis below.

Strong single spin–photon coupling

We now demonstrate strong coupling between a single electron spin and a single photon, as evidenced by the observation of vacuum Rabi splitting. Vacuum Rabi splitting occurs when the transition frequency of a two-level atom f_a is brought into resonance with a cavity photon of frequency f_c (refs 21, 23). Light–matter hybridization leads to two vacuum-Rabi-split peaks in the cavity transmission. For our single-spin qubit, the transition frequency between two Zeeman-split spin states is $f_a \approx E_Z/h$, where $E_Z = g\mu_B B_{tot}$ is the Zeeman energy and the approximate sign is due to spin–charge hybridization, which shifts the qubit frequency slightly. Here g is the g-factor of the electron, μ_B is the Bohr magneton and $B_{tot} = \sqrt{[(B_{x,L}^M + B_{x,R}^M)/2]^2 + (B_z^M + B_z^{ext})^2}$ is the total magnetic field. To bring f_a into resonance with f_c, we vary the external magnetic field B_z^{ext} along the z axis while measuring the cavity transmission spectrum A/A_0 as a function of the drive frequency f (Fig. 2a). Vacuum Rabi splittings are clearly observed at $B_z^{ext} = -91.2$ mT and $B_z^{ext} = 92.2$ mT, indicating that $E_Z/h = f_c$ at these field values and that the single spin is coherently hybridized with a single cavity photon. These measurements are performed on DQD1, with $2t_c/h = 7.4$ GHz and $\varepsilon = 0$. The dependence of g_s on ε and t_c is investigated below[41]. Assuming $g = 2$ for silicon, we estimate that an intrinsic field of about 120 mT is added by the micromagnet, comparable to values found in a previous experiment using a similar cobalt micromagnet design[9].

To further verify the strong spin–photon coupling, we plot the cavity transmission spectrum at $B_z^{ext} = 92.2$ mT (Fig. 2b). The two normal-mode peaks are separated by the vacuum Rabi frequency $2g_s/(2\pi) = 11.0$ MHz, giving an effective spin–photon coupling rate of $g_s/(2\pi) = 5.5$ MHz. The photon decay rate at finite magnetic field is extracted from the line width of A/A_0 at $B_z^{ext} = 90.3$ mT, at which E_Z/h is largely detuned from f_c, yielding $\kappa/(2\pi) = 1.8$ MHz. A spin decoherence rate of $\gamma_s/(2\pi) = 2.4$ MHz, with contributions from both charge

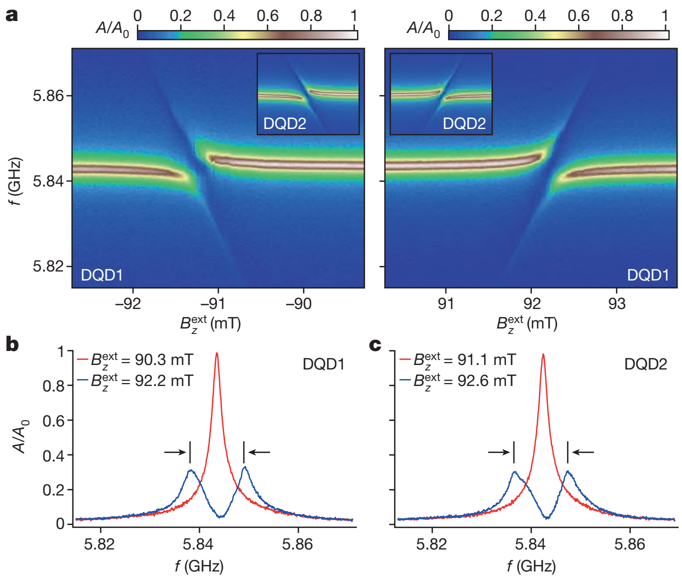

Figure 2 | Strong single spin–photon coupling. a, A/A_0 as a function of the cavity drive frequency f and an externally applied magnetic field B_z^{ext} for DQD1. Insets show data from DQD2 at the same values of t_c and ε and plotted over the same range of f. B_z^{ext} ranges from −94 mT to −91.1 mT (91.1 mT to 94 mT) for the left (right) inset. **b**, A/A_0 as a function of f for DQD1 at $B_z^{\mathrm{ext}} = 90.3$ mT (red) and $B_z^{\mathrm{ext}} = 92.2$ mT (blue) **c**, A/A_0 as a function of f for DQD2 at $B_z^{\mathrm{ext}} = 91.1$ mT (red) and $B_z^{\mathrm{ext}} = 92.6$ mT (blue). In **b** and **c**, the frequency difference between the two transmission peaks, indicated by the black arrows, is 11.0 MHz (**b**) and 10.6 MHz (**c**). The spin–photon coupling rate $g_s/(2\pi)$ corresponds to half the frequency separation and so is 5.5 MHz for DQD1 and 5.3 MHz for DQD2.

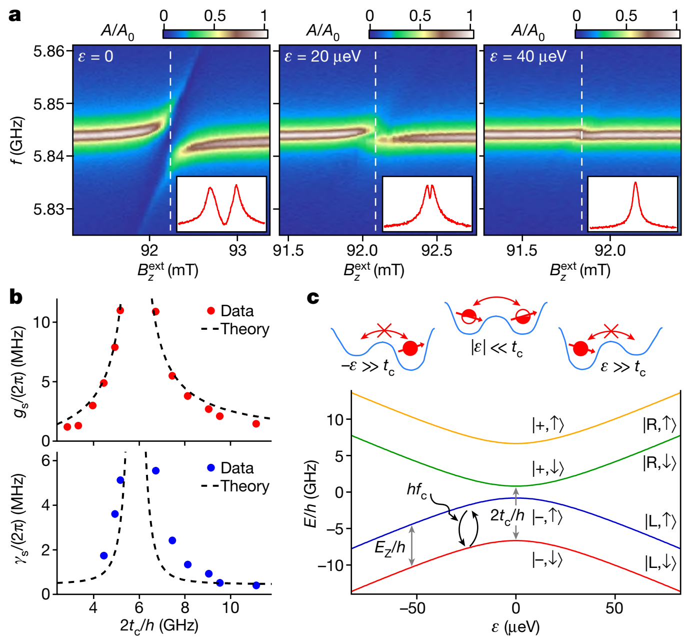

Figure 3 | Electrical control of spin–photon coupling. a, A/A_0 as a function of f and B_z^{ext} at $\varepsilon = 0$ (left), $\varepsilon = 20$ μeV (about 4.8 GHz; middle) and $\varepsilon = 40$ μeV (about 9.7 GHz; right), with $2t_c/h = 7.4$ GHz. Insets show A/A_0 as a function of f at the values of B_z^{ext} indicated by the white dashed lines in the main panels. **b**, Spin–photon coupling rate $g_s/(2\pi)$ (top) and spin decoherence rate $\gamma_s/(2\pi)$ (bottom) as functions of $2t_c/h$, with $\varepsilon = 0$ (data). The dashed lines show theoretical predictions. A potential uncertainty of 0.01–0.1 MHz exists for each value of $g_s/(2\pi)$ and $\gamma_s/(2\pi)$ owing to uncertainties in the locations of the transmission peaks used to determine $g_s/(2\pi)$ (Extended Data Fig. 5) and the widths of the Lorentzian fits used to determine $\gamma_s/(2\pi)$ (Extended Data Fig. 4). **c**, DQD energy levels as a function of ε, calculated with $B_z^{\mathrm{ext}} + B_z^{\mathrm{M}} = 209$ mT, $B_x^{\mathrm{M}} = 15$ mT and $2t_c/h = 7.4$ GHz. Here B_z^{M} denotes the magnetic field produced by the cobalt micomagnet parallel to B_z^{ext}, and B_x^{M} is related to the strength of the inhomogeneous magnetic field perpendicular to B_z^{ext}. The symbols ↑ (↓), L (R) and − (+) denote the quantum states of the electron that correspond to up (down) spin states, left-dot (right-dot) orbital states and molecular bonding (anti-bonding) states, respectively. The schematics at the top illustrate the distribution of the wavefunction of the electron in different regimes of ε. For $\varepsilon \gg t_c$ and $-\varepsilon \gg t_c$, the electron is localized within one dot and tunnelling between the dots is largely forbidden, resulting in a small g_s due to a small effective oscillating magnetic field. For $|\varepsilon| \ll t_c$, the electron may tunnel between the two dots and experience a large oscillating magnetic field due to the spatial field gradient, resulting in a large g_s.

decoherence and magnetic noise from the ^{29}Si nuclei, is extracted from microwave spectroscopy in the dispersive regime with $2t_c/h = 7.4$ GHz and $\varepsilon = 0$ (Extended Data Fig. 4), confirming that the strong-coupling regime $g_s > \gamma_s, \kappa$ has been reached. The spin–photon coupling rate obtained here is more than four orders of magnitude larger than rates currently achievable using direct magnetic-dipole coupling to lumped-element superconducting resonators[30,45].

The local magnetic field that is generated using cobalt micromagnets is very reproducible, as evidenced by examining the other DQD in the cavity. Measurements on DQD2 show vacuum Rabi splittings at $B_z^{\mathrm{ext}} = \pm 92.6$ mT (Fig. 2a, insets). The spin–photon coupling rate and spin decoherence rate are determined to be $g_s/(2\pi) = 5.3$ MHz and $\gamma_s/(2\pi) = 2.4$ MHz, respectively (Fig. 2c). These results are highly consistent with DQD1, and so we henceforth focus on DQD1.

Electrical control of spin–photon coupling

For quantum information applications it is desirable to turn qubit–cavity coupling rapidly on for quantum-state transfer and rapidly off for qubit-state preparation. Rapid control of the coupling rate is often accomplished by quickly modifying the qubit–cavity detuning $f_a - f_c$. Practically, such tuning can be achieved by varying the qubit transition frequency f_a with voltage or flux pulses[46,47] or by using a tunable cavity[20]. These approaches are not directly applicable for control of the spin–photon coupling rate because f_a depends primarily on magnetic fields that are difficult to vary on nanosecond timescales. In this section, we show that control of the spin–photon coupling rate can be achieved electrically by tuning ε and t_c (refs 32, 40).

We first investigate the ε dependence of g_s. In Fig. 3a we show measurements of A/A_0 as a function of B_z^{ext} and f for $\varepsilon = 0$, $\varepsilon = 20$ μeV and $\varepsilon = 40$ μeV. At $\varepsilon = 20$ μeV (about 4.8 GHz), vacuum Rabi splitting is observed at $B_z^{\mathrm{ext}} = 92.1$ mT with a spin–photon coupling rate of $g_s/(2\pi) = 1.0$ MHz that is substantially lower than the value of $g_s/(2\pi) = 5.5$ MHz obtained at $\varepsilon = 0$. At $\varepsilon = 40$ μeV (about 9.7 GHz), only a small dispersive shift is observed in the cavity transmission spectrum at $B_z^{\mathrm{ext}} = 91.8$ mT, suggesting a further decrease in g_s. These observations are qualitatively understood by considering that at $\varepsilon = 0$ the electron is delocalized across the DQD and forms molecular bonding (|−⟩) or anti-bonding (|+⟩) charge states (Fig. 3c). In this regime, the cavity electric field leads to a displacement of the electron wavefunction of the order of 1 nm (Methods)[33]. Consequently, the electron spin experiences a large oscillating magnetic field, resulting in a substantial spin–photon coupling rate. By contrast, with $|\varepsilon| \gg t_c$ the electron is localized within one dot and it is natural to work with a basis of localized electronic wavefunctions |L⟩ and |R⟩, where L and R correspond to the electron being in the left and right dot, respectively (Fig. 3c). In this effectively single-dot regime, the displacement of the electron wavefunction by the cavity electric field is estimated to be about 3 pm for a single-dot orbital energy of $E_{\mathrm{orb}} = 2.5$ meV (ref. 48), greatly suppressing the spin–photon coupling mechanism[33]. The large difference in the effective displacement lengths between the single-dot and double-dot regimes also implies an improvement in the spin–photon coupling rate at $\varepsilon = 0$ of approximately two orders of magnitude compared to $|\varepsilon| \gg t_c$. Alternatively, the reduction of g_s may be

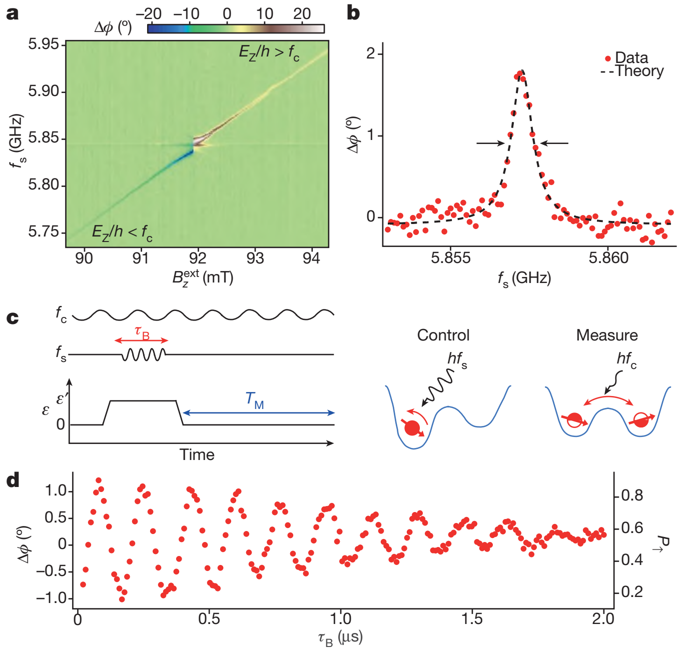

Figure 4 | Quantum control and dispersive readout of a single spin. **a**, Cavity phase response $\Delta\phi$ at $f=f_c$ when gate P1 is driven continuously at a variable frequency f_s and power $P_s=-106$ dBm, with $2t_c/h=9.5$ GHz and $\varepsilon=0$. A background phase response, obtained by measuring $\Delta\phi(B_z^{ext})$ in the absence of a microwave drive on P1, is subtracted from each column of the data to correct for slow drifts in the microwave phase. **b**, Electron spin resonance (ESR) line as measured in $\Delta\phi(f_s)$ at $2t_c/h=11.1$ GHz, $\varepsilon=0$, $B_z^{ext}=92.18$ mT and $P_s=-123$ dBm (data). The dashed line shows a fit to a Lorentzian with a full-width at half-maximum of $\gamma_s/\pi=0.81\pm0.04$ MHz (indicated by the arrows). **c**, Schematic showing the experimental sequence for coherent spin control and measurement. Spin control is performed using a high-power microwave burst when the electron is largely localized within one dot ($|\varepsilon|\gg t_c$) and spin–photon coupling is turned off. Spin-state readout is achieved using the dispersive response of a cavity photon at $\varepsilon=0$ and when spin–photon coupling is turned on. **d**, $\Delta\phi$ as a function of τ_B, with $2t_c/h=11.1$ GHz and $\varepsilon'=70$ μeV, showing single-spin Rabi oscillations. The excited-state population of the spin qubit $P_\uparrow$ is indicated on the right y axis (see Methods).

interpreted as a result of suppressed hybridization between the $|-,\uparrow\rangle$ and $|+,\downarrow\rangle$ states due to their growing energy difference at larger $|\varepsilon|$, as evident from Fig. 3c (see discussion below). Here $\uparrow$ ($\downarrow$) denotes an electron spin that is aligned (anti-aligned) with B_z^{ext}. These measurements highlight the important role of charge hybridization in the DQD.

Additional electric control of g_s is enabled by voltage tuning t_c (Fig. 1f). In Fig. 3b we show $g_s/(2\pi)$ and $\gamma_s/(2\pi)$ as functions of $2t_c/h$ at $\varepsilon=0$, as extracted from vacuum Rabi splitting measurements and microwave spectroscopy of the electron spin resonance (ESR) transition line width (Figs 2b, 4b, Extended Data Figs 4, 5). Both rates increase rapidly as $2t_c/h$ approaches the Larmor precession frequency $E_Z/h\approx5.8$ GHz, and a spin–photon coupling rate as high as $g_s/(2\pi)=11.0$ MHz is found at $2t_c/h=5.2$ GHz. These trends are consistent with the DQD energy-level spectrum shown in Fig. 3c[33,34,41]. With $2t_c/h\gg E_Z/h$ and $\varepsilon=0$, the two lowest energy levels are $|-,\downarrow\rangle$ and $|-,\uparrow\rangle$ and the electric-dipole coupling to the cavity field is small. As $2t_c$ is reduced and made comparable to E_Z, the ground state remains $|-,\downarrow\rangle$ but the excited state becomes an admixture of $|-,\uparrow\rangle$ and $|+,\downarrow\rangle$ owing to the magnetic-field gradient $B_{x,R}^M-B_{x,L}^M=2B_x^M$ and the small energy difference between the states. The quantum transition that is close to resonance with E_Z is now partially composed of a change in charge state from $-$ to $+$, which responds strongly to the cavity electric field and gives rise to larger values of g_s. For $2t_c/h<E_Z/h$, a decrease in t_c increases the energy difference between $|-,\uparrow\rangle$ and $|+,\downarrow\rangle$, which reduces their hybridization and results in a smaller g_s. We note that hybridization with charge states increases the susceptibility of the spin to charge noise and relaxation, resulting in an effective spin decoherence rate γ_s that is also strongly dependent on t_c (Fig. 3b)[33,34,41]. Theoretical predictions of g_s and γ_s as functions of $2t_c/h$, based on measured values of g_c and γ_c (Fig. 1e) are in good agreement with the data (Fig. 3b)[41]. The discrepancy in the fit of γ_s is discussed in Methods. The electric control of spin–photon coupling demonstrated here allows the spin qubit to switch quickly between regimes with strong coupling to the cavity and idle regimes in which the spin–photon coupling rate and susceptibility to charge decoherence are small.

Dispersive readout of a single spin

The preceding measurements demonstrate the ability to couple a single electron spin to a single photon coherently, potentially enabling long-range spin–spin couplings[46,47]. For the device to serve as a building block for a quantum processor, it is also necessary to prepare, control and read out the spin state of the trapped electron deterministically. We first induce spin transitions by driving gate P1 with a continuous microwave tone of frequency f_s and power $P_s=-106$ dBm. When $f_s\approx E_Z/h$, the excited-state population of the spin qubit $P_\uparrow$ increases and the ground state-population $P_\downarrow$ decreases. In the dispersive regime, in which the qubit–cavity detuning $\Delta/(2\pi)\approx E_Z/h-f_c$ satisfies $|\Delta/(2\pi)|\gg g_s/(2\pi)$, the cavity transmission experiences a phase response $\Delta\phi\approx\tan^{-1}[2g_s^2/(\kappa\Delta)]$ for a fully saturated ($P_\uparrow=0.5$) qubit[19,42]. It is therefore possible to measure the spin state of a single electron by probing the cavity transmission. As a demonstration, we spectroscopically probe the ESR transition by measuring $\Delta\phi$ as a function of f_s and B_z^{ext} (Fig. 4a). These data are acquired with $2t_c/h=9.5$ GHz and $\varepsilon=0$. The ESR transition is clearly visible as a narrow feature with $\Delta\phi\neq0$ that shifts to higher f_s with increasing B_z^{ext}. $\Delta\phi$ also changes sign as B_z^{ext} increases, consistent with the sign change of the qubit–cavity detuning Δ when the Larmor precession frequency E_Z/h exceeds f_c. The nonlinear response in the small region around $B_z^{ext}=92$ mT is due to the breakdown of the dispersive condition $|\Delta/(2\pi)|\gg g_s/(2\pi)$.

Finally, we demonstrate coherent single-spin control and dispersive spin-state readout. For these measurements, we choose $\varepsilon=0$ and $2t_c/h=11.1$ GHz to minimize the spin decoherence rate γ_s (Fig. 3b). Here the spin–photon coupling rate $g_s/(2\pi)=1.4$ MHz (Fig. 3b). The external field is fixed at $B_z^{ext}=92.18$ mT, which ensures that the system is in the dispersive regime with $\Delta/(2\pi)=14$ MHz $\gg g_s/(2\pi)$. A measurement of $\Delta\phi(f_s)$ in the low-power limit (Fig. 4b) yields a Lorentzian line shape with a full-width at half-maximum of 0.81 MHz, which corresponds to a low spin decoherence rate of $\gamma_s/(2\pi)=0.41$ MHz (refs 19, 42). Qubit control and measurement are achieved using the pulse sequence illustrated in Fig. 4c. Starting with a spin-down state $|\downarrow\rangle$ at $\varepsilon=0$, the DQD is pulsed to a large detuning $\varepsilon'=70$ μeV (about 17 GHz), which decouples the spin from the cavity. A microwave burst with frequency $f_s=5.874$ GHz, power $P_s=-76$ dBm and duration τ_B is subsequently applied to P1 to drive a spin rotation[9,36,38]. The DQD is then pulsed adiabatically back to $\varepsilon=0$ for a fixed measurement time T_M for dispersive readout. To reinitialize the qubit, we choose $T_M=20$ μs $\gg T_1(\varepsilon=0)$, where $T_1(\varepsilon=0)=3.2$ μs is the spin relaxation time measured at $\varepsilon=0$ (Extended Data Fig. 6). Figure 4d displays the time-averaged $\Delta\phi$ as a function of τ_B, obtained with an integration time of 100 ms for each data point. We observe coherent single-spin Rabi oscillations with a Rabi frequency of $f_R=6$ MHz. In contrast to readout approaches that rely on spin-dependent tunneling[9,38,49], our dispersive cavity-based readout corresponds in principle to quantum non-demolition readout[24]. The readout scheme is also distinct from previous work that used a cavity-coupled InAs DQD, which detects the spin state through Pauli blockade rather than spin–photon coupling[36]. In addition to enabling single spin–photon coupling, our device is capable of preparing, controlling and dispersively reading out single spins.

Conclusion

We have realized a coherent spin–photon interface at which a single spin in a silicon DQD is strongly coupled to a microwave-frequency photon through the combined effects of the electric-dipole interaction and spin–charge hybridization (see Methods for a discussion of the prospects of applying the spin–photon interface to realize cavity-mediated spin–spin coupling). Spin–photon coupling rates of up to 11 MHz are measured in the device, exceeding magnetic-dipole coupling rates by nearly five orders of magnitude. The spin decoherence rate is strongly dependent on the inter-dot tunnel coupling t_c and ranges from 0.4 MHz to 6 MHz, possibly limited by a combination of charge noise, charge relaxation and remnant nuclear field fluctuations. All-electric control of spin–photon coupling and coherent manipulation of the spin state are demonstrated, along with dispersive readout of the single spin, which lays the foundation for quantum non-demolition readout of spin qubits. These results could enable the construction of an ultra-coherent spin quantum computer with photonic interconnects and readout channels, with the capacity for surface codes, 'all-to-all' connectivity and easy integration with other solid-state quantum systems such as superconducting qubits[24,46,47,50–52].

We note that two related preprints appeared after the submission of this Article: ref. 53 presents some of the results discussed here, and ref. 54 explores a different approach to spin–photon coupling and demonstrates coherent coupling of a triple quantum dot to microwave-frequency photons.

Online Content Methods, along with any additional Extended Data display items and Source Data, are available in the online version of the paper; references unique to these sections appear only in the online paper.

1. Tyryshkin, A. M. *et al.* Electron spin coherence exceeding seconds in high-purity silicon. *Nat. Mater.* **11,** 143–147 (2012).
2. Saeedi, K. *et al.* Room-temperature quantum bit storage exceeding 39 minutes using ionized donors in silicon-28. *Science* **342,** 830–833 (2013).
3. Loss, D. & DiVincenzo, D. P. Quantum computation with quantum dots. *Phys. Rev. A* **57,** 120–126 (1998).
4. Petta, J. R. *et al.* Coherent manipulation of coupled electron spins in semiconductor quantum dots. *Science* **309,** 2180–2184 (2005).
5. Neumann, P. *et al.* Multipartite entanglement among single spins in diamond. *Science* **320,** 1326–1329 (2008).
6. Dehollain, J. P. *et al.* Bell's inequality violation with spins in silicon. *Nat. Nanotechnol.* **11,** 242–246 (2016).
7. Zwanenburg, F. A. *et al.* Silicon quantum electronics. *Rev. Mod. Phys.* **85,** 961–1019 (2013).
8. Veldhorst, M. *et al.* An addressable quantum dot qubit with fault-tolerant control-fidelity. *Nat. Nanotechnol.* **9,** 981–985 (2014).
9. Takeda, K. *et al.* A fault-tolerant addressable spin qubit in a natural silicon quantum dot. *Sci. Adv.* **2,** e1600694 (2016).
10. Veldhorst, M. *et al.* A two-qubit logic gate in silicon. *Nature* **526,** 410–414 (2015).
11. Zajac, D. M. *et al.* Resonantly driven CNOT gate for electron spins. *Science* **359,** 439–442 (2018).
12. Watson, T. F. *et al.* A programmable two-qubit quantum processor in silicon. *Nature* https://doi.org/10.1038/nature25766 (2018).
13. McNeil, R. P. G. *et al.* On-demand single-electron transfer between distant quantum dots. *Nature* **477,** 439–442 (2011).
14. Baart, T. A. *et al.* Single-spin CCD. *Nat. Nanotechnol.* **11,** 330–334 (2016).
15. Bertrand, B. *et al.* Fast spin information transfer between distant quantum dots using individual electrons. *Nat. Nanotechnol.* **11,** 672–676 (2016).
16. Flentje, H. *et al.* Coherent long-distance displacement of individual electron spins. *Nat. Commun.* **8,** 501 (2017).
17. Baart, T. A., Fujita, T., Reichl, C., Wegscheider, W. & Vandersypen, L. M. K. Coherent spin-exchange via a quantum mediator. *Nat. Nanotechnol.* **12,** 26–30 (2016).
18. Bruhat, L. E. *et al.* Strong coupling between an electron in a quantum dot circuit and a photon in a cavity. Preprint at https://arxiv.org/abs/1612.05214 (2016).
19. Mi, X., Cady, J. V., Zajac, D. M., Deelman, P. W. & Petta, J. R. Strong coupling of a single electron in silicon to a microwave photon. *Science* **355,** 156–158 (2017).
20. Stockklauser, A. *et al.* Strong coupling cavity QED with gate-defined double quantum dots enabled by a high impedance resonator. *Phys. Rev. X* **7,** 011030 (2017).
21. Thompson, R. J., Rempe, G. & Kimble, H. J. Observation of normal-mode splitting for an atom in an optical cavity. *Phys. Rev. Lett.* **68,** 1132–1135 (1992).
22. Brune, M. *et al.* Quantum Rabi oscillation: a direct test of field quantization in a cavity. *Phys. Rev. Lett.* **76,** 1800–1803 (1996).
23. Wallraff, A. *et al.* Strong coupling of a single photon to a superconducting qubit using circuit quantum electrodynamics. *Nature* **431,** 162–167 (2004).
24. Blais, A., Huang, R.-S., Wallraff, A., Girvin, S. M. & Schoelkopf, R. J. Cavity quantum electrodynamics for superconducting electrical circuits: an architecture for quantum computation. *Phys. Rev. A* **69,** 062320 (2004).
25. Childress, L., Sorensen, A. S. & Lukin, M. D. Mesoscopic cavity quantum electrodynamics with quantum dots. *Phys. Rev. A* **69,** 042302 (2004).
26. Imamoğlu, A. Cavity QED based on collective magnetic dipole coupling: spin ensembles as hybrid two-level systems. *Phys. Rev. Lett.* **102,** 083602 (2009).
27. Schuster, D. I. *et al.* High-cooperativity coupling of electron-spin ensembles to superconducting cavities. *Phys. Rev. Lett.* **105,** 140501 (2010).
28. Amsüss, R. *et al.* Cavity QED with magnetically coupled collective spin states. *Phys. Rev. Lett.* **107,** 060502 (2011).
29. Bienfait, A. *et al.* Controlling spin relaxation with a cavity. *Nature* **531,** 74–77 (2016).
30. Eichler, C. *et al.* Electron spin resonance at the level of 10^4 spins using low impedance superconducting resonators. *Phys. Rev. Lett.* **118,** 037701 (2017).
31. Trif, M., Golovach, V. N. & Loss, D. Spin dynamics in InAs nanowire quantum dots coupled to a transmission line. *Phys. Rev. B* **77,** 045434 (2008).
32. Cottet, A. & Kontos, T. Spin quantum bit with ferromagnetic contacts for circuit QED. *Phys. Rev. Lett.* **105,** 160502 (2010).
33. Hu, X., Liu, Y.-x. & Nori, F. Strong coupling of a spin qubit to a superconducting stripline cavity. *Phys. Rev. B* **86,** 035314 (2012).
34. Beaudoin, F., Lachance-Quirion, D., Coish, W. A. & Pioro-Ladriere, M. Coupling a single electron spin to a microwave resonator: controlling transverse and longitudinal couplings. *Nanotechnology* **27,** 464003 (2016).
35. Frey, T. *et al.* Dipole coupling of a double quantum dot to a microwave resonator. *Phys. Rev. Lett.* **108,** 046807 (2012).
36. Petersson, K. D. *et al.* Circuit quantum electrodynamics with a spin qubit. *Nature* **490,** 380–383 (2012).
37. Viennot, J. J., Dartiailh, M. C., Cottet, A. & Kontos, T. Coherent coupling of a single spin to microwave cavity photons. *Science* **349,** 408–411 (2015).
38. Kawakami, E. *et al.* Electrical control of a long-lived spin qubit in a Si/SiGe quantum dot. *Nat. Nanotechnol.* **9,** 666–670 (2014).
39. Burkard, G. & Imamoglu, A. Ultra-long-distance interaction between spin qubits. *Phys. Rev. B* **74,** 041307 (2006).
40. Jin, P.-Q., Marthaler, M., Shnirman, A. & Schon, G. Strong coupling of spin qubits to a transmission line resonator. *Phys. Rev. Lett.* **108,** 190506 (2012).
41. Benito, M., Mi, X., Taylor, J. M., Petta, J. R. & Burkard, G. Input-output theory for spin-photon coupling in Si double quantum dots. *Phys. Rev. B* **96,** 235434 (2017).
42. Schuster, D. I. *et al.* ac Stark shift and dephasing of a superconducting qubit strongly coupled to a cavity field. *Phys. Rev. Lett.* **94,** 123602 (2005).
43. Mi, X. *et al.* Circuit quantum electrodynamics architecture for gate-defined quantum dots in silicon. *Appl. Phys. Lett.* **110,** 043502 (2017).
44. Mi, X., Peterfalvi, C. G., Burkard, G. & Petta, J. R. High-resolution valley spectroscopy of Si quantum dots. *Phys. Rev. Lett.* **119,** 176803 (2017).
45. Probst, S. *et al.* Inductive-detection electron-spin resonance spectroscopy with 65 spins/$\sqrt{\text{Hz}}$ sensitivity. *Appl. Phys. Lett.* **111,** 202604 (2017).
46. Majer, J. *et al.* Coupling superconducting qubits via a cavity bus. *Nature* **449,** 443–447 (2007).
47. Sillanpää, M. A., Park, J. I. & Simmonds, R. W. Coherent quantum state storage and transfer between two phase qubits via a resonant cavity. *Nature* **449,** 438–442 (2007).
48. Zajac, D. M., Hazard, T. M., Mi, X., Wang, K. & Petta, J. R. A reconfigurable gate architecture for Si/SiGe quantum dots. *Appl. Phys. Lett.* **106,** 223507 (2015).
49. Elzerman, J. M. *et al.* Single-shot read-out of an individual electron spin in a quantum dot. *Nature* **430,** 431–435 (2004).
50. Fowler, A. G., Mariantoni, M., Martinis, J. M. & Cleland, A. N. Surface codes: towards practical large-scale quantum computation. *Phys. Rev. A* **86,** 032324 (2012).
51. Debnath, S. *et al.* Demonstration of a small programmable quantum computer with atomic qubits. *Nature* **536,** 63–66 (2016).
52. Nigg, S. E., Fuhrer, A. & Loss, D. Superconducting grid-bus surface code architecture for hole-spin qubits. *Phys. Rev. Lett.* **118,** 147701 (2017).
53. Samkharadze, N. *et al.* Strong spin-photon coupling in silicon. Preprint at https://arxiv.org/abs/1711.02040 (2017).
54. Landig, A. J. *et al.* Coherent spin-qubit photon coupling. Preprint at https://arxiv.org/abs/1711.01932 (2017).

Acknowledgements We thank A. J. Sigillito for technical assistance and M. J. Gullans for discussions. This work was supported by the US Department of Defense under contract H98230-15-C0453, Army Research Office grant W911NF-15-1-0149, and the Gordon and Betty Moore Foundations EPiQS Initiative through grant GBMF4535. Devices were fabricated in the Princeton University Quantum Device Nanofabrication Laboratory.

Author Contributions X.M. fabricated the sample and performed the measurements. X.M., D.M.Z. and J.R.P. developed the design and fabrication process for the DQD. X.M. and S.P. developed the niobium cavity fabrication process. M.B., G.B., J.M.T. and J.R.P. developed the theory for the experiment. X.M., M.B. and J.M.T. analysed the data. X.M., J.R.P., G.B. and J.M.T. wrote the manuscript with input from the other authors. J.R.P. planned and supervised the experiment.

Author Information Reprints and permissions information is available at www.nature.com/reprints. The authors declare competing financial interests: details are available in the online version of the paper. Readers are welcome to comment on the online version of the paper. Publisher's note: Springer Nature remains neutral with regard to jurisdictional claims in published maps and institutional affiliations. Correspondence and requests for materials should be addressed to J.R.P. (petta@princeton.edu).

Reviewer Information *Nature* thanks T. Meunier and the other anonymous reviewer(s) for their contribution to the peer review of this work.

METHODS

Device fabrication and measurement. The Si/SiGe heterostructure consists of a 4-nm-thick Si cap, a 50-nm-thick $Si_{0.7}Ge_{0.3}$ spacer layer, a 8-nm-thick natural-Si quantum well and a 225-nm-thick $Si_{0.7}Ge_{0.3}$ layer on top of a linearly graded $Si_{1-x}Ge_x$ relaxed buffer substrate. Design and fabrication details for the superconducting cavity and DQDs are described elsewhere[43]. The approximately 200-nm-thick Co micromagnet is defined using electron beam lithography and lift off. In contrast to earlier devices, the gate filter for P1 was changed to an L_1–C–L_2 filter, with $L_1=4$ nH, $C=1$ pF and $L_2=12$ nH (ref. 43). This three-segment filter allows microwave signals below 2.5 GHz to pass with less than 3 dB of attenuation.

All data are acquired in a dilution refrigerator with a base temperature of 10 mK and electron temperature of $T_e=60$ mK. The measurements of the transmission amplitude and phase response of the cavity (Figs 1, 4) are performed using a homodyne detection scheme[23]. The measurements of the transmission spectra of the cavity (Figs 2, 3) are performed using a network analyser. The microwave drive applied to P1 (Fig. 4) is provided by a vector microwave source and the detuning pulses are generated by an arbitrary waveform generator, which also controls the timing of the microwave burst (Fig. 4d).

To maximize the magnetization of the Co micromagnet and minimize hysteresis, data at positive (negative) external applied magnetic fields (Fig. 2a) are collected after $B_z^{\rm ext}$ is first ramped to a large value of $+300$ mT (-300 mT). A small degree of hysteresis still remains for the micromagnet of DQD1, as can be seen by the different magnitudes of $B_z^{\rm ext}$ at which positive- and negative-field vacuum Rabi splittings are observed (Fig. 2a). In Fig. 4a, the slope of the ESR transition is $d(E_Z/h)/dB_z^{\rm ext}=44$ MHz mT^{-1}, which is higher than the value (28 MHz mT^{-1}) expected for a fully saturated micromagnet. The slope of the transition suggests that the micromagnet is not fully magnetized and has a magnetic susceptibility of $dB_z^{\rm M}/dB_z^{\rm ext}\approx 0.6$ around $B_z^{\rm ext}=92$ mT.

Estimate of displacement length. The displacement length of the electron wavefunction by the cavity electric field may be estimated by considering the spin–photon coupling strength. For $g_s/(2\pi)=10$ MHz, the effective AC magnetic field $B_{\rm ac}^{\rm ESR}$ that drives ESR is $B_{\rm ac}^{\rm ESR}=[g_s/(2\pi)][h/(g\mu_B)]\approx 0.4$ mT. The field gradient for our DQD is $2B_x^{\rm M}/l\approx 0.3$ mT nm^{-1}, where $l=100$ nm is the inter-dot distance. Therefore, the effective displacement of the electron wavefunction is estimated to be about 1 nm in the DQD regime. For a single dot, the spin–photon coupling strength is expected to be $g_s/(2\pi)\approx(g\mu_B B_x^{\rm M}/E_{\rm orb})(g_c/2\pi)\approx 30$ kHz (refs 31, 33) for an orbital energy of $E_{\rm orb}=2.5$ meV (ref. 48). The equivalent AC magnetic field that is induced by the cavity is therefore $B_{\rm ac}^{\rm ESR}\approx 1$ μT, corresponding to a displacement length of only about 3 pm.

Conversion of cavity phase response to spin population. For the dispersive readout of the Rabi oscillations (Fig. 4d), the theoretically expected cavity phase response is $\phi_\uparrow=\tan^{-1}[2g_s^2/(\kappa\Delta)]=9.6°$ when the spin qubit is in the excited state, and $\phi_\downarrow=-\tan^{-1}[2g_s^2/(\kappa\Delta)]=-9.6°$ when the spin qubit is in the ground state[42,55]. Because our measurement is averaged over $T_M\gg T_1$, spin relaxation during readout will reduce the phase contrast observed in the experiment. To enable a conversion between the phase response of the cavity $\Delta\phi$ and the excited-state population of the spin qubit $P_\uparrow$, we measure the spin relaxation time T_1 by fixing the microwave burst time at $\tau_B=80$ ns, which corresponds to a π pulse on the spin qubit. The phase response of the cavity $\Delta\phi$ is then measured as a function of T_M for $T_M>5$ μs $>T_1$ (Extended Data Fig. 6). The result is fitted to a function of the form $\Delta\phi=\phi_0+\phi_1(T_1/T_M)[1-\exp(-T_M/T_1)]$ to extract $T_1=3.2$ μs, where ϕ_0 and ϕ_1 are additional fitting parameters[36]. We have ignored the effects of the cavity ringdown time $1/\kappa\approx 90$ ns and the π-pulse time of 80 ns in the fit, because both of these times are much shorter than the measurement time T_M. The phase contrast that results from the fit, $\phi_1\approx 17.7°$, is close to the maximum contrast expected at this spin–photon detuning, $\phi_\uparrow-\phi_\downarrow=19.2°$. On the basis of this value of T_1, we convert the measured phase response into the excited-state population via $P_\uparrow=(1+\Delta\phi/\phi_{\uparrow,r})/2$, where $\phi_{\uparrow,r}=\phi_\uparrow(T_1/T_M)[1-\exp(-T_M/T_1)]=1.5°$ is the reduced phase response due to spin relaxation during the readout time $T_M=20$ μs. The converted spin population $P_\uparrow$ shown in Fig. 4d has a visibility of about 70%, which could be improved by performing single-shot measurements[55].

Input–output theory for cavity transmission. Here we briefly summarize the theoretical methods used to calculate the cavity transmission A/A_0 shown in Fig. 1e and Extended Data Fig. 7; see ref. 41 for a detailed description of the theory. We start from the Hamiltonian that describes the DQD

$$H_0=\frac{1}{2}(\varepsilon\tau_z+2t_c\tau_x+B_z\sigma_z+B_x^{\rm M}\sigma_x\tau_z)\qquad(1)$$

where τ_x and τ_z are Pauli operators that act on the orbital charge states of the DQD electron, σ_x and σ_z are Pauli operators that act on the spin states of the electron, $B_z=B_z^{\rm ext}+B_z^{\rm M}$ denotes the total magnetic field along the z axis and $B_x^{\rm M}=(B_{x,\rm R}^{\rm M}-B_{x,\rm L}^{\rm M})/2$ is half the magnetic field difference of the DQD in the x direction. In the theoretical model, we have assumed that the average magnetic field in the x direction satisfies $(B_{x,\rm R}^{\rm M}+B_{x,\rm L}^{\rm M})/2=0$, which is a good approximation given the geometry of the micromagnet and its alignment with the DQD. We add the electric-dipole coupling to the cavity with the Hamiltonian

$$H_I=g_c(a+a^\dagger)\tau_z$$

where a and $a^\dagger$ are the photon operators for the cavity. The electric-dipole operator can be expressed in the eigenbasis $\{|n\rangle\}$ of H_0 as

$$\tau_z=\sum_{n,m=0}^{3}d_{nm}|n\rangle\langle m|$$

We then write the quantum Langevin equations for the operators a and $\sigma_{nm}=|n\rangle\langle m|$:

$$\begin{aligned}\dot a&=i\Delta_0 a-\frac{\kappa}{2}a+\sqrt{\kappa_1}a_{\rm in,1}+\sqrt{\kappa_2}a_{\rm in,2}-ig_c e^{i\omega_R t}\sum_{n,m=0}^{3}d_{nm}\sigma_{nm}\\ \dot\sigma_{nm}&=-i(E_m-E_n)\sigma_{nm}-\sum_{n'm'}\gamma_{nm,n'm'}\sigma_{n'm'}+\sqrt{2\gamma}F\\ &\quad-ig_c(ae^{-i\omega_R t}+a^\dagger e^{i\omega_R t})d_{mn}p_{nm}\end{aligned}\qquad(2)$$

where $\Delta_0=\omega_R-\omega_c$ is the detuning of the driving field frequency ($\omega_R=2\pi f$) relative to the cavity frequency ($\omega_c=2\pi f_c$) and $p_{nm}=p_n-p_m$ is the population difference between levels n and m (p_n can, for example, be assumed to be a Boltzmann distribution in thermal equilibrium). This description is equivalent to a more general master-equation approach in the weak-driving regime in which population changes in the DQD can be neglected. Furthermore, κ_1 and κ_2 are the photon decay rates at ports 1 and 2 of the cavity and $a_{\rm in,1}$ is the input field of the cavity, which we assume to couple through port 1 only ($a_{\rm in,2}=0$). The quantum noise of the DQD F is neglected in what follows. The super-operator γ with matrix elements $\gamma_{nm,n'm'}$ represents decoherence processes, including charge relaxation and dephasing due to charge noise (these processes also imply some degree of spin relaxation and dephasing due to spin–charge hybridization via $B_x^{\rm M}$). Our goal is to relate the incoming parts $a_{{\rm in},i}$ of the external field at the ports to the outgoing fields $a_{{\rm out},i}=\sqrt{\kappa_i}a-a_{{\rm in},i}$. The transmission $A=\bar a_{\rm out,2}/\bar a_{\rm in,1}$ (where the overbars denote time-averaged expectation values) through the microwave cavity is then computed using a rotating-wave approximation to eliminate the explicit time dependence in equation (2), by solving the equations for the expected value of these operators in the stationary limit ($\bar a$ and $\bar\sigma_{n,m}$):

$$A=\frac{-i\sqrt{\kappa_1\kappa_2}}{-\Delta_0-i\kappa/2+g_c\sum_{n=0}^{2}\sum_{j=1}^{3-n}d_{n,n+j}\chi_{n,n+j}}$$

where $\chi_{n,n+j}=\bar\sigma_{n,n+j}/\bar a$ are the single-electron partial susceptibilities and d_{ij} are the dipole-transition matrix elements between DQD states.

Theoretical models for spin–photon coupling and spin decoherence. Here we present a brief derivation of the analytical expressions for the spin–photon coupling rate g_s and the spin decoherence rate γ_s. A more extensive discussion of spin–photon coupling and spin decoherence specific to our device architecture is presented in ref. 41. We focus on the $\varepsilon=0$ regime used in Fig. 3b. Accounting for spin–charge hybridization due to the field gradient $B_x^{\rm M}$, the relevant eigenstates of the DQD Hamiltonian in equation (1) are $|0\rangle\approx|-,\downarrow\rangle$, $|1\rangle=\cos(\Phi/2)|-,\uparrow\rangle+\sin(\Phi/2)|+,\downarrow\rangle$, $|2\rangle=\sin(\Phi/2)|-,\uparrow\rangle-\cos(\Phi/2)|+,\downarrow\rangle$ and $|3\rangle\approx|+,\uparrow\rangle$. Here we have introduced a mixing angle $\Phi=\tan^{-1}[g\mu_B B_x^{\rm M}/(2t_c-g\mu_B B_z)]$. The dipole-transition matrix element for the primarily spin-like transition between $|0\rangle$ and $|1\rangle$ is $d_{01}\approx-\sin(\Phi/2)$ and the dipole-transition matrix element for the primarily charge-like transition between $|0\rangle$ and $|2\rangle$ is $d_{02}\approx\cos(\Phi/2)$. The transition between $|0\rangle$ and $|3\rangle$ is too high in energy (off-resonance) and is therefore excluded from our model. The spin–photon coupling rate is $g_s=g_c|d_{01}|=g_c|\sin(\Phi/2)|$, in agreement with previous theoretical results[33,34].

To calculate the effective spin decoherence rate $\gamma_s^{(c)}$ that arises from charge decoherence, we first construct the operators $\sigma_{01}=|0\rangle\langle 1|\approx\cos(\Phi/2)\sigma_s+\sin(\Phi/2)\sigma_r$ and $\sigma_{02}=|0\rangle\langle 2|\approx\sin(\Phi/2)\sigma_s-\cos(\Phi/2)\sigma_r$. Here $\sigma_s=|-,\downarrow\rangle\langle -,\uparrow|$ and $\sigma_r=|-,\downarrow\rangle\langle +,\downarrow|$ are lowering operators for the electron spin and charge, respectively. Assuming that the electron charge states have a constant decoherence rate $\gamma_c=\gamma_1/2+\gamma_\phi$, where γ_1 is the charge relaxation rate and γ_ϕ is a dephasing rate due to charge noise[56], the equations of motion for these operators are

$$\dot\sigma_{01}=\gamma_c\left[-\sin^2\left(\frac{\Phi}{2}\right)\sigma_{01}+\frac{\sin(\Phi)}{2}\sigma_{02}\right]$$

$$\dot\sigma_{02}=\gamma_c\left[\frac{\sin(\Phi)}{2}\sigma_{01}-\cos^2\left(\frac{\Phi}{2}\right)\sigma_{02}\right]$$

Combined with charge–photon coupling, the overall equations of motion (equation (2)) in a rotating frame with a drive frequency $f \approx f_c$ assume the form

$$\dot{a} = i\Delta_0 a - \frac{\kappa}{2}a + \sqrt{\kappa_1}\, a_{\text{in},1} - ig_c(d_{01}\sigma_{01} + d_{02}\sigma_{02})$$

$$\dot{\sigma}_{01} = -i\delta_1\sigma_{01} - \gamma_c \sin^2\left(\frac{\Phi}{2}\right)\sigma_{01} + \gamma_c \frac{\sin(\Phi)}{2}\sigma_{02} - ig_c a d_{10}$$

$$\dot{\sigma}_{02} = -i\delta_2\sigma_{02} - \gamma_c \cos^2\left(\frac{\Phi}{2}\right)\sigma_{02} + \gamma_c \frac{\sin(\Phi)}{2}\sigma_{01} - ig_c a d_{20}$$

The δ_1 and δ_2 terms are defined as $\delta_1/(2\pi) = (E_1 - E_0)/h - f$ and $\delta_2/(2\pi) = (E_2 - E_0)/h - f$, where $E_{0,1,2}$ correspond to the energy of the $|0\rangle$, $|1\rangle$ and $|2\rangle$ state, respectively. Steady-state solutions to the above equations give the electric susceptibility of the spin qubit transition $\chi_{0,1} = \sigma_{01}/a = g_s/(\delta_1 - i\gamma_s^{(c)})$, where we have identified a charge-induced spin decoherence rate $\gamma_s^{(c)} = \gamma_c[\delta_2 \sin^2(\Phi/2) + \delta_1 \cos^2(\Phi/2)]/\delta_2$. To account for spin dephasing due to fluctuations of the ^{29}Si nuclear spin bath, we express the total spin decoherence rate assuming a Voigt profile:

$$\gamma_s = \frac{\gamma_s^{(c)}}{2} + \sqrt{\left(\frac{\gamma_s^{(c)}}{2}\right)^2 + 8\ln 2\left(\frac{1}{T^*_{2,\text{nuclear}}}\right)^2}$$

where $T^*_{2,\text{nuclear}} \approx 1$ μs is the electron-spin dephasing time due to nuclear field fluctuations[11,38].

When fitting the data in Fig. 3b, we use the experimentally determined values of $g_c/(2\pi) = 40$ MHz and $\gamma_c/(2\pi) = 35$ MHz, along with the best-fitting field gradient $B_x^{\text{M}} = 15$ mT. For every t_c, the fitted value for B_z is adjusted so that the spin-qubit frequency $(E_1 - E_0)/h$ matches the cavity frequency f_c exactly. The slight discrepancy between theory and experiment for γ_s could be due to the frequency dependence of γ_c, changes in γ_c with B_z^{ext} or other decoherence mechanisms that are not captured by this simple model. To resolve such a discrepancy, a complete measurement of γ_c as a function of $2t_c/h$ and the external field B_z^{ext} is needed.

The complete theory[41] also allows $g_s/(2\pi)$ to be calculated for non-zero values of ε. Using $2t_c/h = 7.4$ GHz, we estimate $g_s/h = 2.3$ MHz at $\varepsilon = 20$ μeV (about 4.8 GHz), close to the value of $g_s/h = 1.0$ MHz measured at this DQD detuning (Fig. 3a).

In this theoretical model, we have ignored Purcell decay of the spin qubit through the cavity[29]. This is justified because γ_s at every value of t_c is measured with a large spin–cavity detuning $\Delta \approx 10g_s$. The expected Purcell decay rate of the spin qubit is $\Gamma_P/(2\pi) = [\kappa g_s^2/(\kappa^2/4 + \Delta^2)]/(2\pi) \approx 0.02$ MHz, well below the measured values of $\gamma_s/(2\pi)$. We also note that, at least in the $2t_c \gg E_Z$ limit, spin decoherence at $\varepsilon = 0$ is dominated by noise-induced dephasing rather than by energy relaxation. This is because at $2t_c/h = 11.1$ GHz the spin decoherence rate $\gamma_s/(2\pi) = 0.41$ MHz corresponds to a coherence time of $T_2 = 0.4$ μs $\ll 2T_1 = 6.4$ μs.

Line shapes of vacuum Rabi splittings. In contrast to charge–photon systems[19,20,23], the two resonance modes in the vacuum Rabi splittings (Fig. 2b, c) show slightly unequal widths. This effect can be seen by comparing the observed spectrum of DQD1 with the expected behaviour of an equivalent two-level charge qubit that is coupled strongly to a cavity, calculated using a master-equation simulation with thermal photon number $n_{\text{th}} = 0.02$ (black dashed line in Extended Data Fig. 7). The unequal widths are unlikely to be a result of a large thermal photon number in the cavity, because the transmission spectrum calculated with $n_{\text{th}} = 0.5$ (orange dashed line) clearly does not fit the experimental data[57].

Instead, the observed asymmetry probably arises from the dispersive interaction between the cavity and the primarily charge-like transition between $|0\rangle$ and $|2\rangle$, which results in three-level dynamics that is more complicated than the two-level dynamics that characterizes charge–photon systems. A more complete treatment of this effect is given in ref. 41. Here we compare the experimental observation with theory by calculating $A(f)/A_0$ using $g_c/(2\pi) = 40$ MHz (DQD1) or $g_c/(2\pi) = 37$ MHz (DQD2), $\gamma_c/(2\pi) = 105$ MHz (DQD1) or $\gamma_c/(2\pi) = 130$ MHz (DQD2), $\kappa/(2\pi) = 1.8$ MHz, tunnel couplings $2t_c/h = 7.4$ GHz, $B_x^{\text{M}} = 15$ mT and $B_z = 209.6$ mT. The results are shown as black solid lines alongside experimental data in Extended Data Fig. 7. The agreement between experiment and theory is very good for both devices. In particular, the asymmetry between the vacuum Rabi modes is also seen in the theoretical calculations. The larger values of γ_c used in the theoretical calculations may again be due to the frequency dependence of γ_c or to changes in γ_c with B_z^{ext}. Further experiments are needed to resolve this difference.

Prospects for long-range spin–spin coupling. The coherent spin–photon interface may be readily applied to enable spin–spin coupling across the cavity bus. Here we evaluate two possible schemes for implementing such a coupling, both of which have been demonstrated with superconducting qubits[46,47]. The first approach uses direct photon exchange to perform quantum-state transfer between two qubits[47]. The transfer protocol starts by tuning qubit 1 into resonance with the unpopulated cavity for a time $1/(4g_s)$, at the end of which the state of qubit 1 is transferred completely to the cavity. Qubit 1 is then detuned rapidly from the cavity and qubit 2 is brought into resonance with the cavity for a time $1/(4g_s)$, at the end of which the state of qubit 1 is transferred completely to qubit 2. Therefore, the time required for quantum-state transfer across the cavity is $1/(2g_s)$. Because the decay of vacuum Rabi oscillations occurs at a rate $\kappa/2 + \gamma_s$, the threshold for coherent-state transfer between two spin qubits is $2g_s/(\kappa/2 + \gamma_s) > 1$. The ratio $2g_s/(\kappa/2 + \gamma_s)$ is plotted as a function of $2t_c/h$ in Extended Data Fig. 8a. It can be seen that $2g_s/(\kappa/2 + \gamma_s) > 1$ for all values of $2t_c/h$, indicating that spin–spin coupling via real photon exchange is achievable and may be implemented at any value of t_c. For our device parameters, the regime $2t_c/h \approx 6$ GHz, in which spin–charge hybridization is large and the ratio $2g_s/(\kappa/2 + \gamma_s)$ reaches a maximum of 3.5, seems most advantageous for such a coupling scheme.

The second approach to spin–spin coupling uses virtual photon exchange[46]. In this scheme, both spin qubits would operate in the dispersive regime, with an effective coupling rate of $J = g_s^2(1/\Delta_1 + 1/\Delta_2)/2$, where Δ_1 and Δ_2 are the qubit–cavity detunings for qubits 1 and 2, respectively. Assuming that both qubits operate with an equal detuning $\Delta_{1,2} = 10g_s$ to minimize Purcell decay, $J = g_s/10$. For coherent spin–spin interaction, $J > \gamma_s$ needs to be satisfied, leading to the condition $g_s/\gamma_s > 10$. In Extended Data Fig. 8b, we plot the ratio g_s/γ_s as a function of $2t_c/h$, observing a maximum of $g_s/\gamma_s \approx 4$ at $2t_c/h \approx 10$ GHz. Because the dominant spin mechanism is probably hyperfine-induced dephasing by the ^{29}Si nuclei in this regime (the decoherence rate $\gamma_s/(2\pi) \approx 0.4$ MHz is close to the decoherence rates commonly found with single-spin qubits in natural Si; ref. 38), transitioning to isotopically purified ^{28}Si host materials is likely to lead to an order-of-magnitude reduction in $\gamma_s/(2\pi)$, as demonstrated recently[58]. Such an improvement will allow virtual-photon-mediated spin–spin coupling to be implemented in our device architecture as well.

Last, we note that both coupling approaches will benefit substantially from larger values of the charge–photon coupling rate g_c, which is achievable through the development of higher-impedance cavities[20,59]. The superconducting cavity used here is estimated to have an impedance between 200 Ω and 300 Ω. Increasing this value to about 2 kΩ, which is possible by using NbTiN as the superconducting material, will lead to another factor-of-three increase in g_c and therefore g_s. This could enable the $g_s/\gamma_s > 100$ regime to be accessed, where high-fidelity two-qubit gates can be implemented between distant spins. Improvements in the fidelity of cavity-mediated two-qubit gates, particularly in the case of real photon exchange, can also be sought by improving the quality factor of the cavity (and thereby reducing κ). This is achievable by implementing stronger gate line filters[43] and removing lossy dielectrics such as the atomic-layer-deposited Al_2O_3 underneath the cavity.

Data availability. The data that support the findings of this study are available from the corresponding author on reasonable request. Source Data for Figs 1–4 and Extended Data Figs 2–8 are available with the online version of the paper.

55. Wallraff, A. *et al.* Approaching unit visibility for control of a superconducting qubit with dispersive readout. *Phys. Rev. Lett.* **95,** 060501 (2005).
56. Wallraff, A., Stockklauser, A., Ihn, T., Petta, J. R. & Blais, A. Comment on "Vacuum Rabi splitting in a semiconductor circuit QED system". *Phys. Rev. Lett.* **111,** 249701 (2013).
57. Rau, I., Johansson, G. & Shnirman, A. Cavity quantum electrodynamics in superconducting circuits: Susceptibility at elevated temperatures. *Phys. Rev. B* **70,** 054521 (2004).
58. Yoneda, J. *et al.* A >99.9% fidelity quantum-dot spin qubit with coherence limited by charge noise. Preprint at https://arxiv.org/abs/1708.01454 (2017).
59. Samkharadze, N. *et al.* High-kinetic-inductance superconducting nanowire resonators for circuit QED in a magnetic field. *Phys. Rev. Appl.* **5,** 044004 (2016).

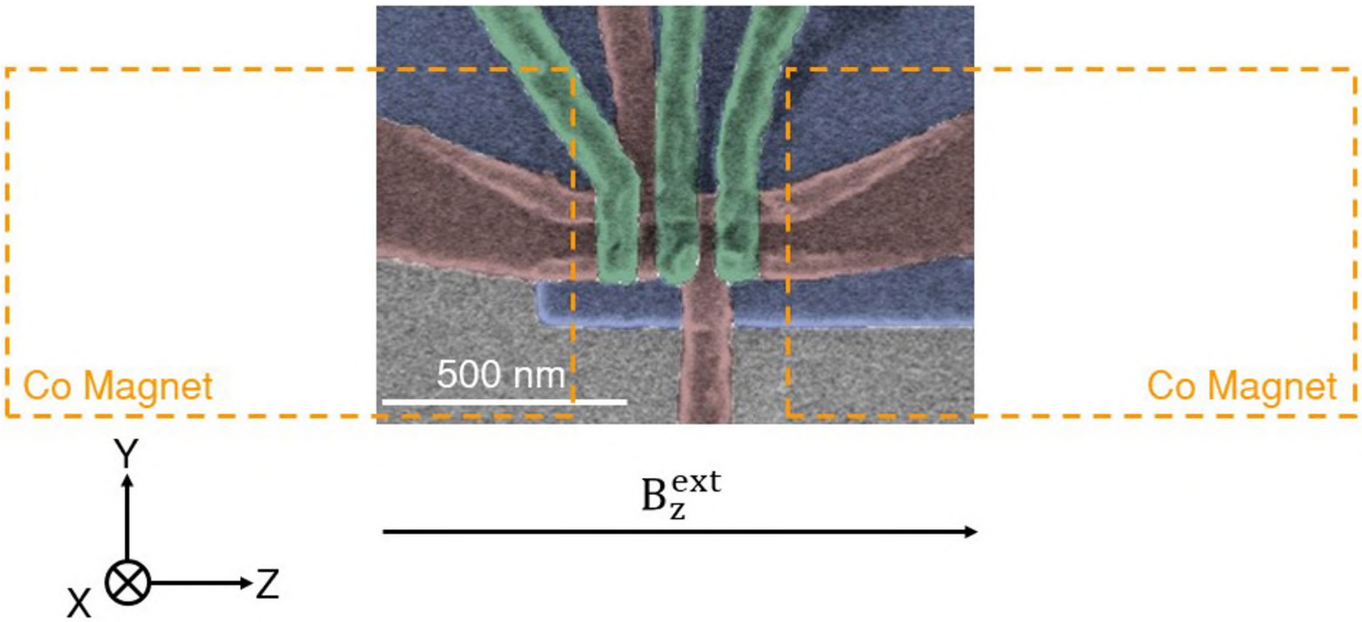

Extended Data Figure 1 | Micromagnet design. To-scale drawing of the micromagnet design, superimposed on top of the SEM image of the DQD. The coordinate axes and the direction of the externally applied magnetic field B_z^{ext} are indicated at the bottom. In this geometry, the DQD electron experiences a homogeneous z field $B_z \approx B_z^{ext} + B_z^{M}$. The total x field B_x that is experienced by the electron is spatially dependent, being approximately $B_{x,L}^{M}$ ($B_{x,R}^{M}$) when the electron is in the L (R) dot ($|\varepsilon| \gg t_c$) and $(B_{x,L}^{M} + B_{x,R}^{M})/2$ when the electron is delocalized between the DQDs ($\varepsilon = 0$). The y field B_y for the DQD electron is expected to be small compared to the other field components for this magnet design.

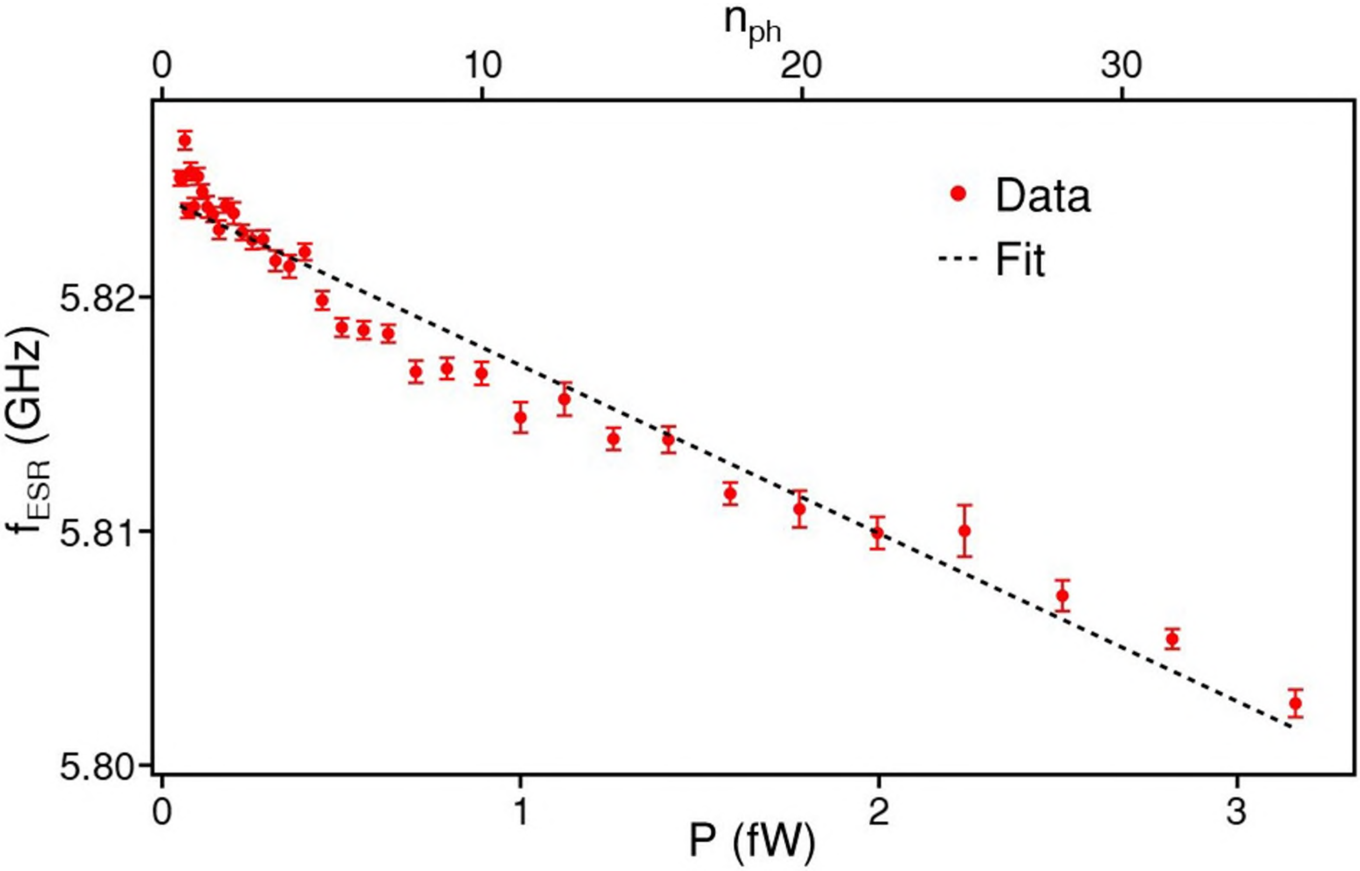

Extended Data Figure 2 | Photon number calibration. The ESR resonance frequency f_{ESR}, measured using the phase response of the cavity $\Delta\phi$ in the dispersive regime (Fig. 4b), is plotted as a function of the estimated power at the input port of the cavity P (data). The device is configured with $g_s/(2\pi) = 2.4$ MHz and spin–photon detuning $\Delta/(2\pi) \approx -18$ MHz. The dashed line shows a fit to $f_{ESR} = f_{ESR}(P=0) + (2n_{ph}g_s^2/\Delta)/(2\pi)$, where n_{ph} is the average number of photons in the cavity, plotted as the top x axis. The experiments are conducted with $P \approx -133$ dBm (0.05 fW), which corresponds to $n_{ph} \approx 0.6$. The error bars indicate the uncertainties in the centre frequency of the ESR transition.

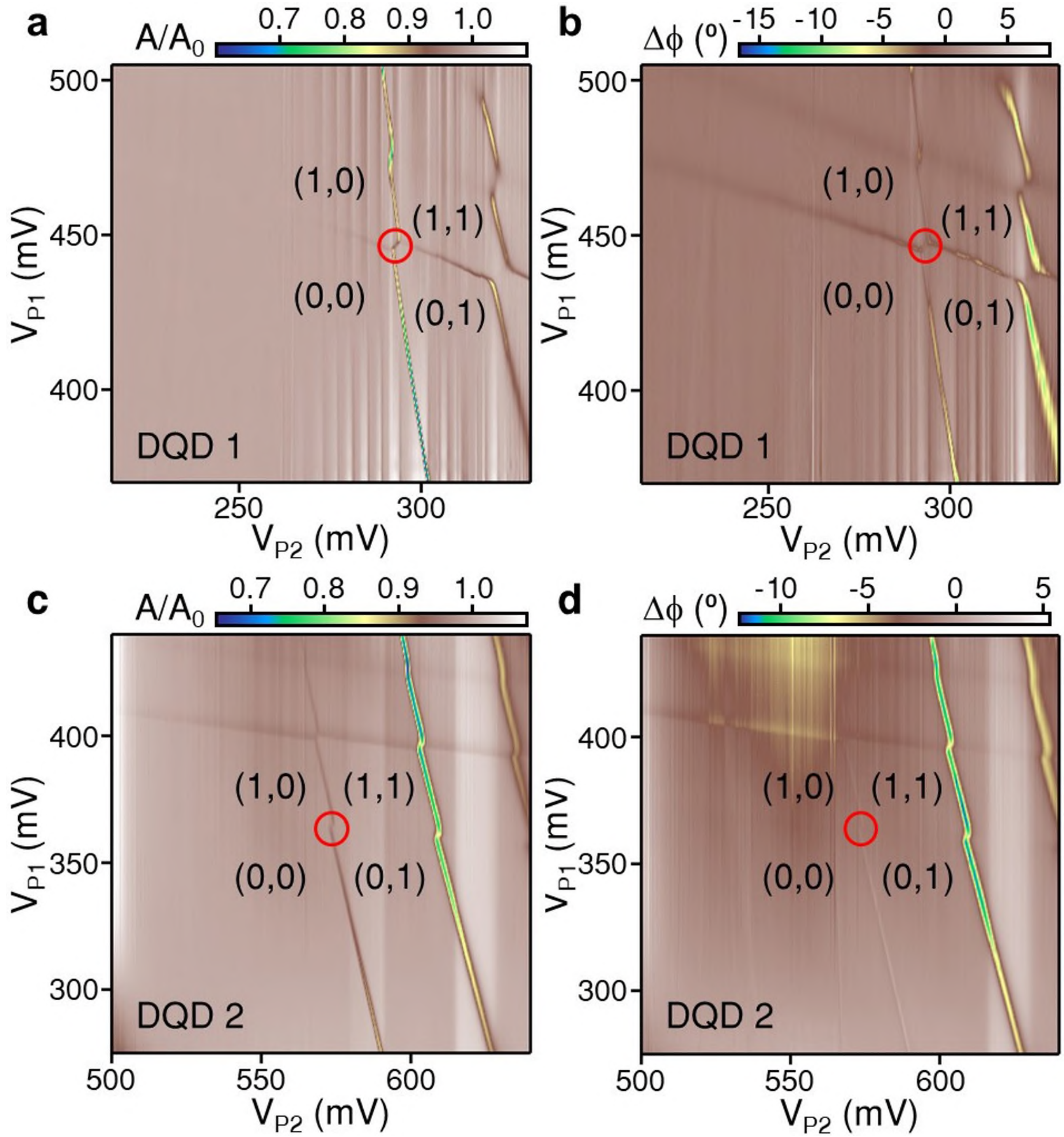

Extended Data Figure 3 | DQD stability diagrams. The cavity transmission amplitude A/A_0 (**a**, **c**) and phase response $\Delta\phi$ (**b**, **d**) are plotted as functions of V_{P1} and V_{P2} for DQD1 (**a**, **b**) and DQD2 (**c**, **d**), obtained with $f = f_c$. The $(1, 0) \leftrightarrow (0, 1)$ transitions are clearly identified on the basis of these measurements and subsequently tuned close to resonance with the cavity for the experiments described in the main text. The red circles indicate the locations of the $(1, 0) \leftrightarrow (0, 1)$ transitions of the two DQDs.

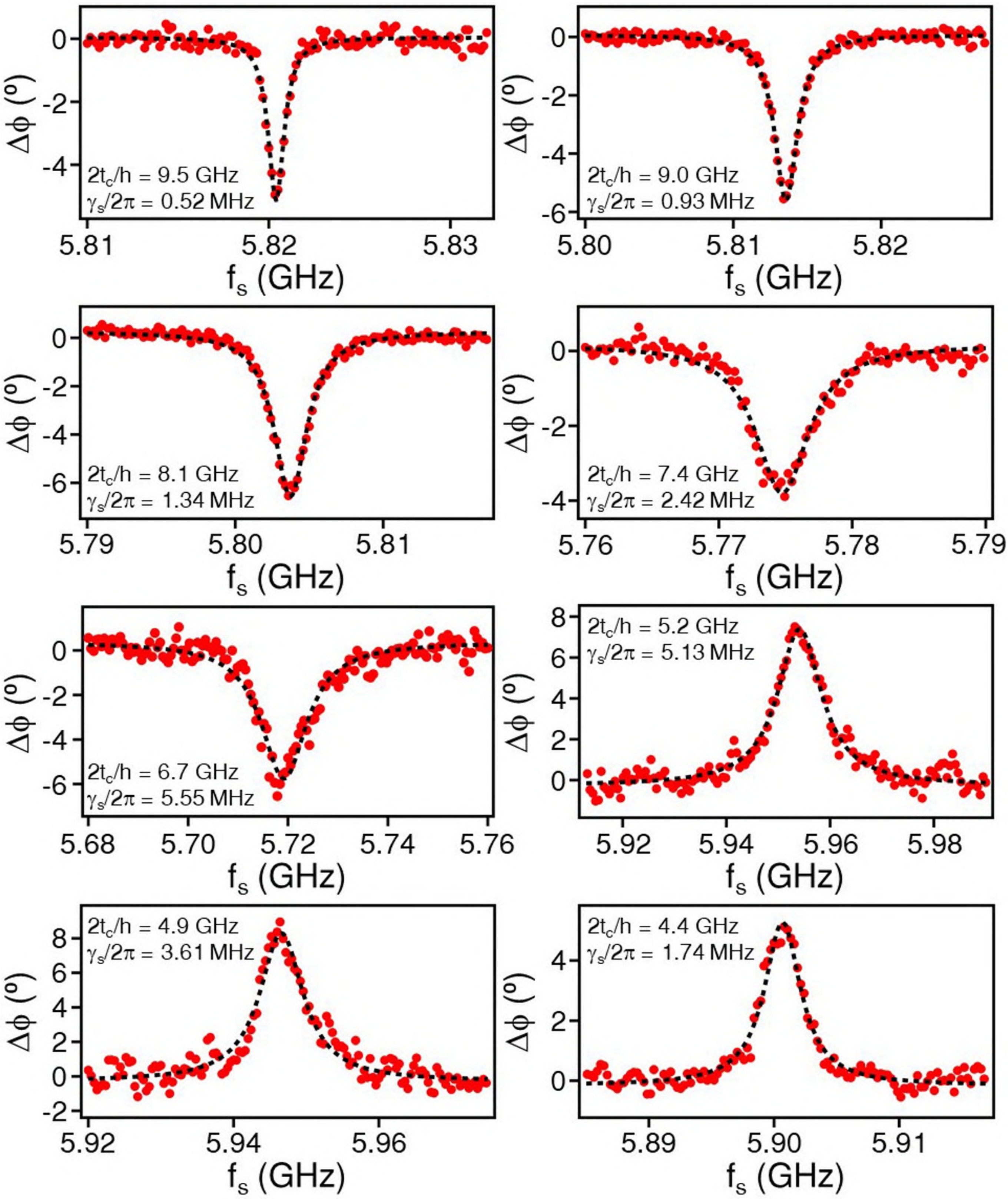

Extended Data Figure 4 | Spin decoherence rates at different DQD tunnel couplings. ESR line, as measured in the cavity phase response $\Delta\phi(f_s)$, is shown for different values of $2t_c/h$ in the low-power limit (data). $\varepsilon = 0$ for every dataset. Dashed lines are fits with Lorentzian functions and $\gamma_s/(2\pi)$ is determined as the half-width at half-maximum of each Lorentzian. The spin–photon detuning $|\Delta| \approx 10\,g_s$ for each dataset, to ensure that the system is in the dispersive regime.

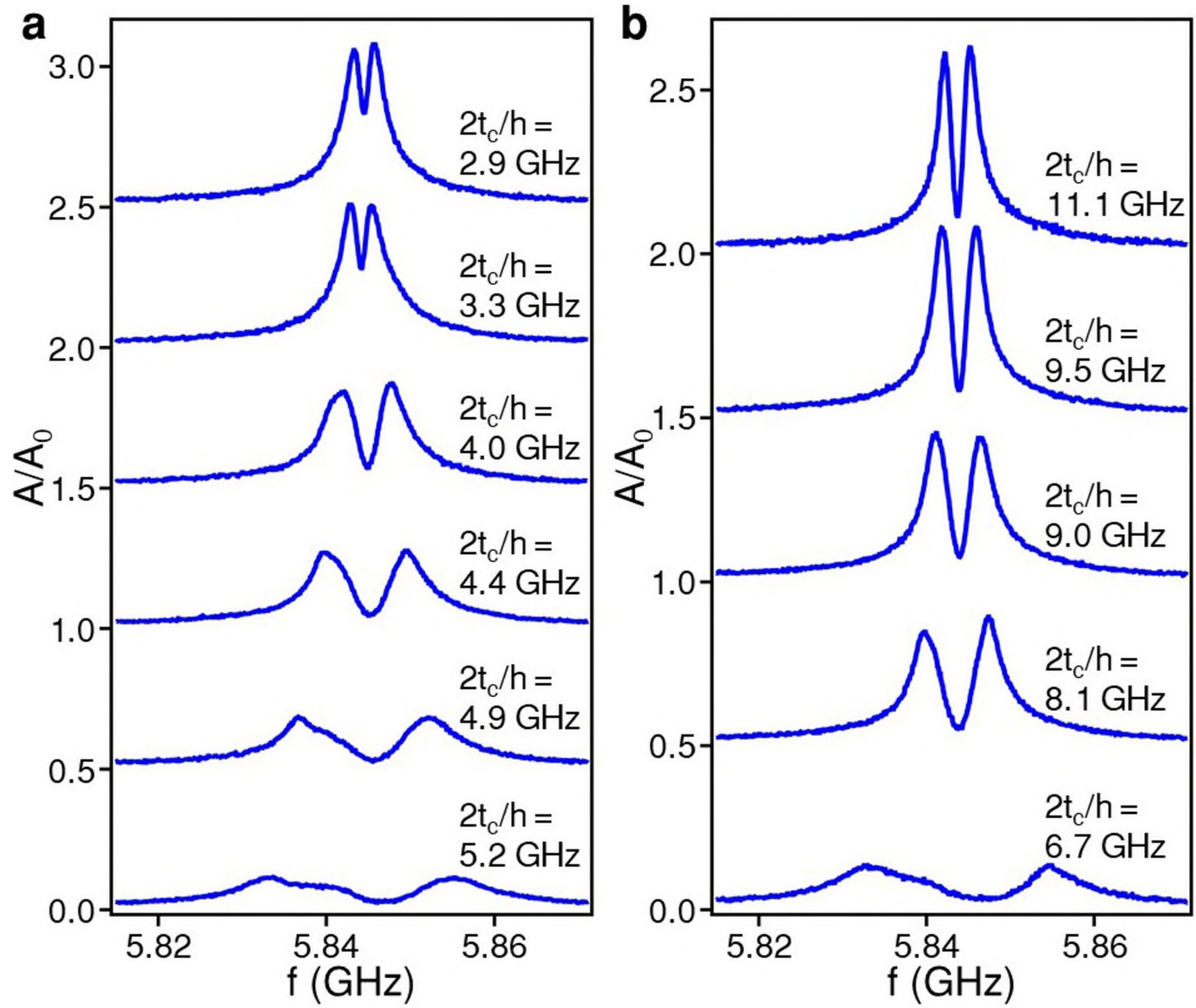

Extended Data Figure 5 | Spin–photon coupling strengths at different DQD tunnel couplings. a, **b**, Vacuum Rabi splittings for $2t_c/h < f_c$ (**a**) and $2t_c/h > f_c$ (**b**), obtained by varying B_z^{ext} until a pair of resonance peaks with approximately equal heights emerges in the cavity transmission spectrum A/A_0. $g_s/(2\pi)$ is then estimated as half the frequency difference between the two peaks. $\varepsilon = 0$ for every dataset. g_s is difficult to measure for $5.2\,\mathrm{GHz} < 2t_c/h < 6.7\,\mathrm{GHz}$ owing to the small values of A/A_0 that arise from the large spin decoherence rates γ_s in this regime.

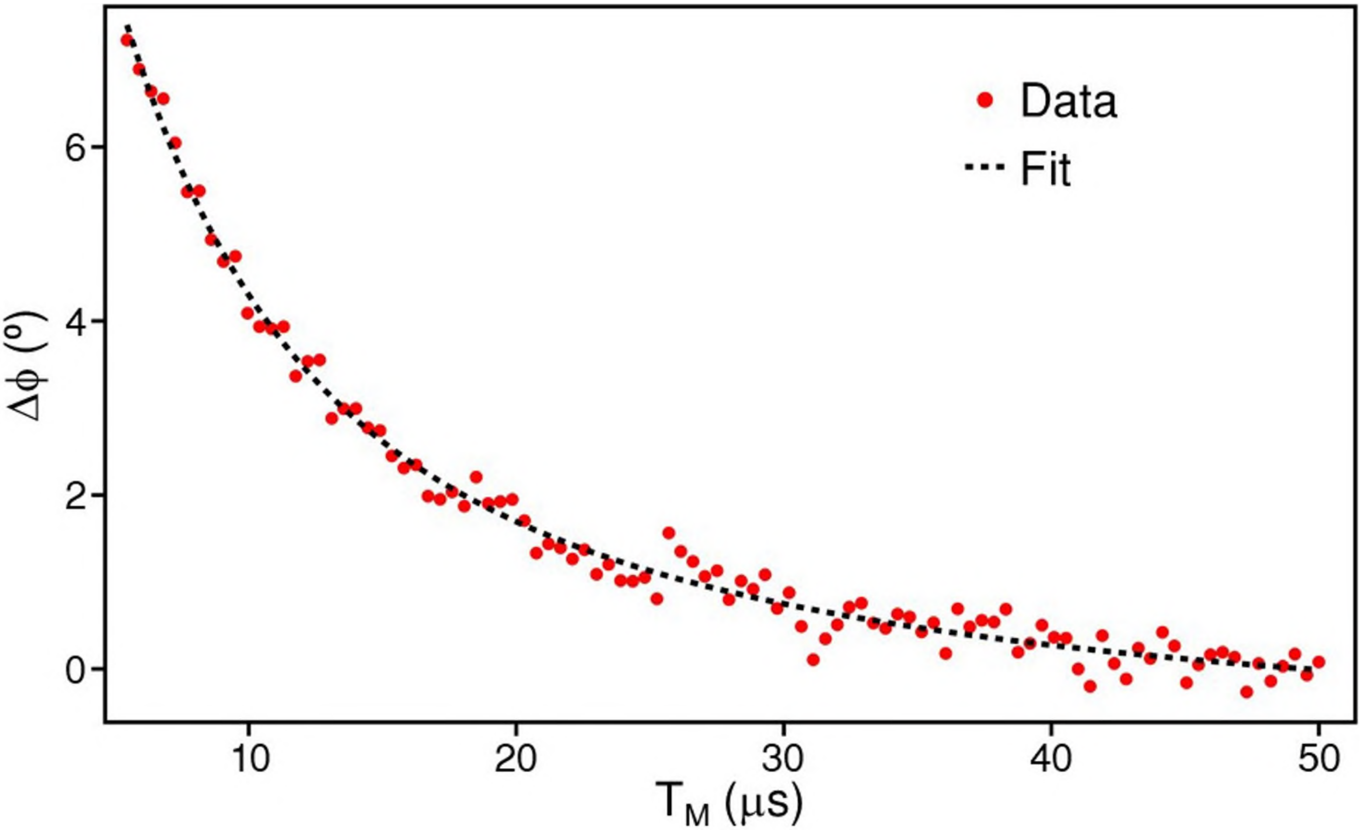

Extended Data Figure 6 | Spin relaxation at $\varepsilon = 0$. The time-averaged phase response of the cavity $\Delta\phi$ is shown as a function of wait time T_{M} (data), measured using the pulse sequence illustrated in Fig. 4c. The microwave burst time is fixed at $\tau_{\mathrm{B}} = 80$ ns. The dashed line shows a fit using the function $\phi_0 + \phi_1(T_1/T_{\mathrm{M}})[1 - \exp(-T_{\mathrm{M}}/T_1)]$, which yields a spin relaxation time of $T_1 \approx 3.2\,\mu$s. The experimental conditions are the same as for Fig. 4d.

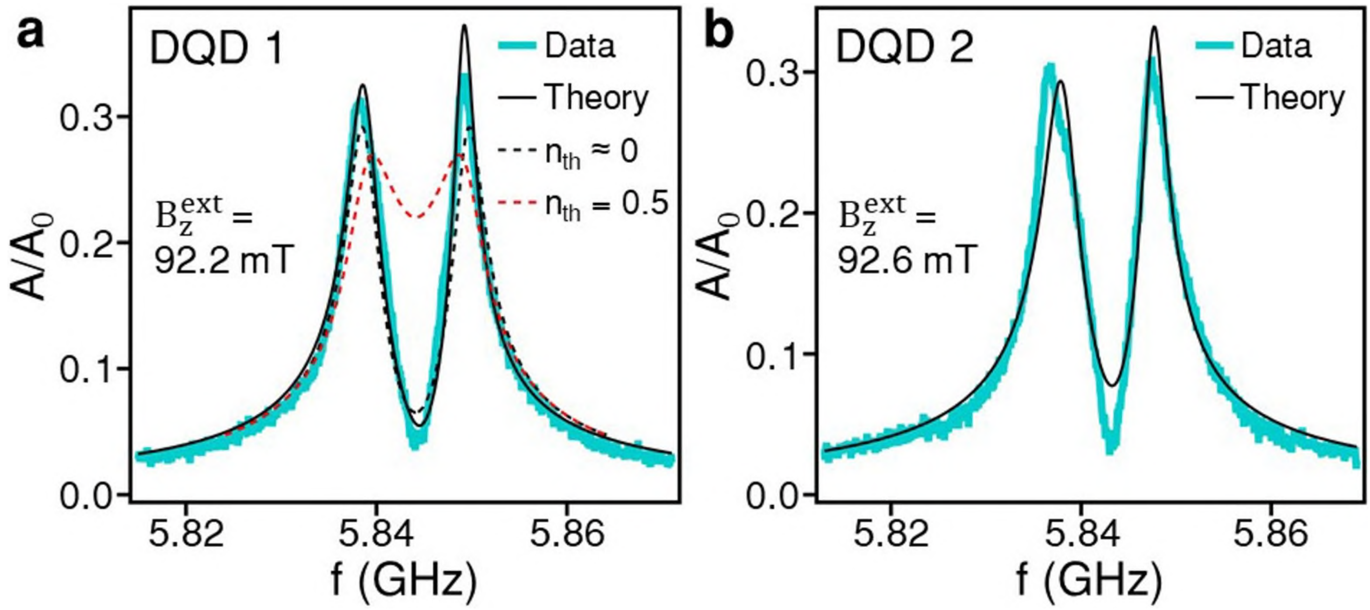

Extended Data Figure 7 | Theoretical fits to vacuum Rabi splittings. The calculated cavity transmission spectra (black solid lines) are superimposed on the experimentally measured vacuum Rabi splittings shown in Fig. 2b, c (data). The calculations are produced with $g_c/(2\pi) = 40\,\mathrm{MHz}$ ($g_c/(2\pi) = 37\,\mathrm{MHz}$), $\kappa/(2\pi) = 1.8\,\mathrm{MHz}$, $\gamma_c/(2\pi) = 105\,\mathrm{MHz}$ ($\gamma_c/(2\pi) = 120\,\mathrm{MHz}$), $B_z = B_z^{\mathrm{ext}} + B_z^{\mathrm{M}} = 209$ mT, $B_x^{\mathrm{M}} = (B_{x,\mathrm{R}}^{\mathrm{M}} - B_{x,\mathrm{L}}^{\mathrm{M}})/2 = 15$ mT and $2t_c/h = 7.4\,\mathrm{GHz}$ for DQD1 (DQD2). For comparison, $A(f)/A_0$, simulated for a two-level charge qubit with a decoherence rate of $\gamma_c/(2\pi) = 2.4\,\mathrm{MHz}$ coupled to a cavity with $\kappa/(2\pi) = 1.8\,\mathrm{MHz}$ at a rate $g_c/(2\pi) = 5.5\,\mathrm{MHz}$, is shown in **a** for thermal photon numbers of $n_{\mathrm{th}} = 0.02$ (black dashed line) and $n_{\mathrm{th}} = 0.5$ (red dashed line).

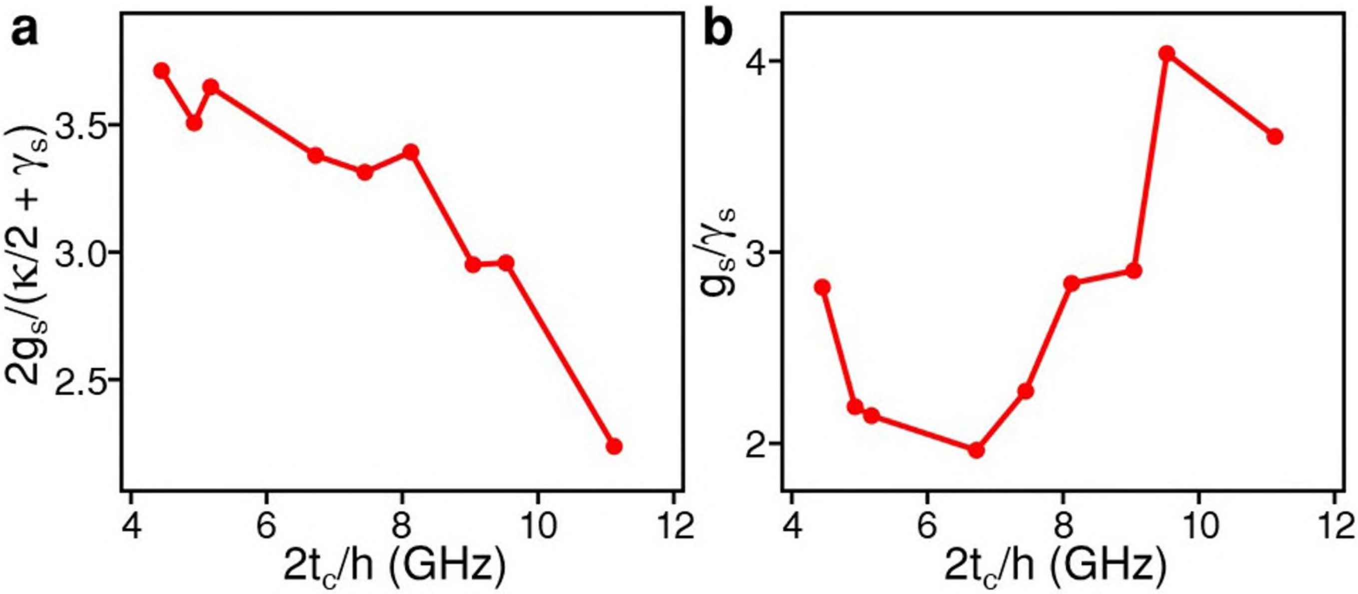

Extended Data Figure 8 | Prospect for long-range spin–spin coupling. a, The ratio $2g_s/(\kappa/2+\gamma_s)$ as a function of $2t_c/h$, calculated using the data in Fig. 3b and $\kappa/(2\pi) = 1.8$ MHz. **b**, The ratio g_s/γ_s as a function of $2t_c/h$, also calculated using the data in Fig. 3b.